nature climate change

SUPPLEMENTARY INFORMATION

https://doi.org/10.1038/s41558-019-0630-6

In the format provided by the authors and unedited.

Increasing impacts of extreme droughts on vegetation productivity under climate change

Chonggang Xu[1]*, Nate G. McDowell[2], Rosie A. Fisher[3,4], Liang Wei[1,5], Sanna Sevanto[1], Bradley O. Christoffersen[6], Ensheng Weng[7] and Richard S. Middleton[1]

[1]Earth and Environmental Sciences Division, Los Alamos National Laboratory, Los Alamos, NM, USA. [2]Earth Systems Analysis and Modeling Division, Pacific Northwest National Laboratory, Richland, WA, USA. [3]Climate and Global Dynamics, National Center for Atmospheric Research, Boulder, CO, USA. [4]Centre Européen de Recherche et de Formation Avancée en Calcul Scientifique, Toulouse, France. [5]Key Laboratory of Western China's Environmental Systems, College of Earth and Environmental Sciences, Lanzhou University, Lanzhou, China. [6]Department of Biology and School of Earth, Environmental, and Marine Sciences, The University of Texas Rio Grande Valley, Edinburg, TX, USA. [7]Center for Climate Systems Research, Columbia University and NASA Goddard Institute for Space Studies, New York, NY, USA. *e-mail: cxu@lanl.gov

Supplementary Notes, Tables and Figures for

INCREASING IMPACTS OF EXTREME DROUGHTS ON VEGETATION PRODUCTIVITY UNDER CLIMATE CHANGE

Chonggang Xu[1*], Nate G. McDowell[2], Rosie A. Fisher[3, 4], Liang Wei[1, 5], Sanna Sevanto[1], Bradley O. Christoffersen[6], Ensheng Weng[7], Richard Middleton[1]

Correspondence to: cxu@lanl.gov

This PDF file includes:

Supplementary Note 1: Definitions of droughts based on plant accessible soil water (PASW)

For a grid cell with longitude *i* and latitude *j* at month *m* of the year *t*, we calculated the PASW for PFT *f* as follows,

$$\mathrm{PASW_m}(i,j,t,f) = \sum_{s_i=1}^{n_s} w_{s_i}(f)\,\mathrm{SW}_{s_i} \qquad \text{(S1.1)}$$

where $w_{s_i}(f)$ is the root fraction of PFT f at soil layer S_i. See Supplementary Note 7 for details of root distribution within different ESMs. SW_{s_i} is the soil water (kg/m^2) at soil layer S_i. For a specific month *m* and a specific PFT *f* at the grid cell with longitude *i* and latitude *j*, we calculated the 2nd, 5th and 10th percentiles of PASW (i.e., $\mathrm{PASW}_m^{(2)}(i,j,f)$, $\mathrm{PASW}_m^{(5)}(i,j,f)$, and $\mathrm{PASW}_m^{(10)}(i,j,f)$) based on the empirical probability function estimated from values of $\mathrm{PASW}_m(i,j,t,f)$ with *t*=1, …,150 for the historical period of year 1850-1999. These percentiles were then used to define droughts for all the study period during 1850-2099 (*t*=1, …, 250). Specifically, we identified month *m* of year *t* is drought month if

$$\mathrm{PASW}_m(i,j,t,f) < \mathrm{PASW}_m^{(10)}(i,j,f), \text{ for } t = 1,\ldots, 250, \qquad \text{(S1.2)}$$

and expected GPP for these drought months is significant lower than expected GPP for non-drought months. Namely, we have,

$$\mathrm{E}(\mathrm{GPP}_m(i,j,t^d,f)) < \mathrm{E}(\mathrm{GPP}_m(i,j,t^{nd},f)), \qquad \text{(S1.3)}$$

where t^d indicates years as defined as droughts and t^{nd} indicates years as defined as non-drought based on eq. (S1.2). We used the Welch Two Sample t-test[1] to test if $\mathrm{E}(\mathrm{GPP}_m(i,j,t^d,f))$ is significant lower than $\mathrm{E}(\mathrm{GPP}_m(i,j,t^{nd},f))$ at significance level of 0.01. For the non-drought impacted months, we chose one out of every 5 years to reduce the impact of temporal auto-correlations among samples on the statistical test. See Supplementary Figs. 11-12 for the number of months selected for the drought analysis. We further classified the drought months into mild droughts if

$$\mathrm{PASW}_m^{(5)}(i,j,f) \le \mathrm{PASW}_m(i,j,t,f) < \mathrm{PASW}_m^{(10)}(i,j,f), \qquad \text{(S1.4)}$$

moderate droughts if

$$\mathrm{PASW}_m^{(2)}(i,j,f) \le \mathrm{PASW}_m(i,j,t,f) < \mathrm{PASW}_m^{(5)}(i,j,f), \qquad \text{(S1.5)}$$

and extreme droughts if

$$\mathrm{PASW}(i,j,t,f) < \mathrm{PASW}_m^{(2)}(i,j,f). \quad \text{(S1.6)}$$

If the same year t was are identified as droughts for different PFTs (e.g., f_1 and f_2) for month m, then the drought category was defined based on the PFT with the lowest p-value of Welch Two Sample T-test for eq. (S1.3), which had the strongest control of PASW on GPP.

Supplementary Note 2: Smoothing spline and stand error estimation

The smoothing spline is a method of fitting a smooth curve to a set of noisy observations[2]. The spline is used to minimize an objective function that considers both goodness of fit of the curve to observations and smoothness of the curve. Namely, we have

$$L(s, \lambda) = \sum_{i=1}^{n} (y_i - s(x_i)) + \lambda \int s''(x) dx \ , \qquad \text{(S2.1)}$$

where L is the objective function of spline $S(x)$ with a smoothness compensation cost of λ, given observations of $(x_i, y_i)[i=1, \ldots, n]$. $s''(x)$ is the second derivative of the spline that represents the smoothness of the curve. The solution of the above objective function is the spline s that minimize L given a specific value of λ. The smoothing spline is a linear estimator[3]. Namely, there is a n by n smoother matrix $H(\lambda)=\{ h_{ij}(\lambda) \}\ [i, j=1, \ldots, n]$ that transform the response vector $Y = < y_i > [i=1, \ldots, n]$ into a vector of fitted value $S = < \hat{s}(x_i) > [i=1, \ldots, n]$ [3]. Specifically,

$$S = H(\lambda)\, Y \ . \qquad \text{(S2.2)}$$

The term $h_{ij}(\lambda)$ determines how much influence of y_j on the fit to y_i (i.e., $\hat{s}(x_i)$). Following linear regressions, $h_{ii}(\lambda)$ is generally termed leverage values that measure the impact of y_i on the fit to y_i (i.e., $\hat{s}(x_i)$). Using the leverage values, we were able to estimate the standard error of the spline $\hat{s}(x_i)$ using the jackknife residuals as follows[2],

$$\hat{\sigma}_i = \sqrt{h_{ii} \mathrm{V}\left(\frac{y_i - \hat{s}(x_i)}{1 - h_{ii}}\right)} \ , \qquad \text{(S2.3)}$$

where $\mathrm{V}(\cdot)$ indicates the function of variance.

In our study, the above response variable y_i was the modeled output (i.e., GPP, temperature, air humidity, precipitation or radiations) from 1850-2099 for a specific month, while the dependent variable x_i represented years. For a specific month m in a grid cell at

longitude *i* and latitude *j*, we had a spline $S_m(i,j)$ based on model outputs $Y_m(i,j,t)$ during years 1850-2099. Namely,

$$S_m(i,j) = H_m(\lambda(i,j))\, Y_m(i,j). \qquad \text{(S2.4)}$$

where $Y_m(i,j) = < Y_m(i,j,t) >$. $H_m(\lambda(i,j)) = \{h_{t_1,t_2}(\lambda(i,j))\}$ $[t_1,\ t_2 = 1,\ \ldots, 250]$. Correspondingly, its standard error at time *t* was estimated as follows,

$$\hat{\sigma}_m^{(s)}(i,j,t) = \sqrt{h_{tt} V(\frac{Y_m(i,j,t) - \hat{s}_m(i,j,t)}{1-h_{tt}})}. \qquad \text{(S2.5)}$$

In order to reduce the impact of temporal autocorrelation on standard error estimation, we only chose one out of every 5 years of $Y_m(i,j,t)$ and $\hat{s}_m(i,j,t)$ [t=1, …, 250] to estimate $V(\frac{Y_m(i,j,t) - \hat{s}_m(i,j,t)}{1-h_{tt}})$.

Many statistical packages are available to compute the smoothing spline. In this study, we used the "smooth.spline" function in R package[2] to estimate splines in view that it is simple and fast and thus suits well for large scale applications like we conducted in this study. The "smooth.spline" function automatically selects the best λ by leave-one-out cross-validations. Namely, the code used all the data except with one observation x_i left out to build a candidate $s'(x)$ given a specific λ'. This $s'(x)$ was then used to predict the leave-out observation y_i and assess its fit. The process was repeated for each of the observational data and finally assessed the overall model fit to all the data given the cost coefficient λ'.

Supplementary Note 3: Estimation of drought impacts

The grid-cell-specific drought-associated change (or deviation) in model output *Y* for month *m* ($d_m^{(\mathrm{d})}(i,j,t)$) was estimated based on the difference between the drought month GPP and its spline estimation. Namely,

$$\hat{d}_m^{(\mathrm{d})}(i,j,t^d) = Y_m(i,j,t^d) - \hat{s}_m(i,j,t^d), \qquad \text{(S3.1)}$$

where $Y_m(i,j,t^d)$ is the modeled output for a specific drought month *m* in a grid cell at longitude *i* and latitude *j*.

The global change in model output *Y* by a specific type of droughts [$\hat{d}^{(\mathrm{d})}(p)$] for a period *p* from year T_{p0} to year T_p can then be summarized as follows,

$$\hat{d}^{(\mathrm{d})}(p) = \frac{\sum_{m=1}^{12}\sum_{t=T_{p0}}^{T_p}\sum_{i=1}^{N_i}\sum_{j=1}^{Nj} I_v(i,j) I_d(i,j,t) \hat{d}_m^{(\mathrm{d})}(i,j,t) A(i,j)}{12(T_p - T_{p0} + 1)\sum_{i=1}^{N_i}\sum_{j=1}^{Nj} I_v(i,j) A(i,j)}, \qquad \text{(S3.2)}$$

where $I_v(i,j)$ is the indictor function for vegetation (1 with vegetation and 0 without vegetation). $I_d(i,j,t)$ is the indictor function for the specific drought (1 with drought and 0 without drought). $A(i,j)$ is the area (m^2) of grid cell at longitude *i* and latitude *j*. The corresponding standard errors of $\hat{d}^{(\mathrm{d})}(p)$, $\hat{\sigma}_{sp}^{(\mathrm{d})}(p)$, were then estimated as follows,

$$\hat{\sigma}_{sp}^{(\mathrm{d})}(p) = \frac{\sqrt{\sum_{m=1}^{12}\sum_{t=T_{p0}}^{T_p}\sum_{i=1}^{N_i}\sum_{j=1}^{Nj} I_v(i,j) I_d(i,j,t)\, \hat{\sigma}_m^{(d)\,2}(i,j,t) A^2(i,j)}}{12(T_p - T_{p0} + 1)\sum_{i=1}^{N_i}\sum_{j=1}^{Nj} I_v(i,j) A(i,j)}, \qquad \text{(S3.3)}$$

where $\hat{\sigma}_m^{(d)\,2}(i,j,t)$ is the variance of $\hat{d}_m^{(\mathrm{d})}(i,j,t)$. It was estimated as follows,

$$\hat{\sigma}_m^{(d)\,2}(i,j,t) = V(\hat{d}_m^{(\mathrm{d})}(i,j)) + \hat{\sigma}_m^{(s)\,2}(i,j,t), \qquad \text{(S3.4)}$$

where $V(\hat{d}_m^{(\mathrm{d})}(i,j))$ is the sample variance of $\hat{d}_m^{(\mathrm{d})}(i,j,t)$. $\hat{\sigma}_m^{(s)\,2}(i,j,t)$ was estimated from eq. (S2.5).

Supplementary Note 4: Importance of different factors to drought-associated GPP anomalies

Using eq. (S2.4) in Supplementary Note 2, for drought month *m* as defined by PASW of PFT f, we estimated mean PASW[$s\mathrm{PASW}_m(i,j,t,f)$], GPP [$s\mathrm{GPP}_m(i,j,t,f)$], air temperature [$s\mathrm{TAS}_m(i,j,t,f)$], air humidity [$s\mathrm{HURS}_m(i,j,t,f)$], precipitation [$s\mathrm{PR}_m(i,j,t,f)$], and radiation [$s\mathrm{RSDS}_m(i,j,t,f)$]. Then, using eq. (S3.1) in Supplementary Note 3, we estimated the drought-associated deviations (or anomalies) for drought month *m* and PFT f in PASW [$d\mathrm{PASW}_m(i,j,t,f)$], in GPP [$d\mathrm{GPP}_m(i,j,t,f)$], in air temperature [$d\mathrm{TAS}_m(i,j,t,f)$], in air humidity [$d\mathrm{HURS}_m(i,j,t,f)$], in precipitation [$d\mathrm{PR}_m(i,j,t,f)$], and in radiation [$d\mathrm{RSDS}_m(i,j,t,f)$]. To understand the impact of different climate and environmental factors on the GPP anomalies, we applied a multilinear regression to values of $d\mathrm{GPP}_m(i,j,t,f)$ with different climate variables at the global scale for years within a specific 25-year period (*t*). Meanwhile vegetation composition and status (e.g., leaf area index) could also play a very important role on GPP deviation (or anomaly) associated with droughts. In this study, we were not able to compile comprehensive complete vegetation states for all models due to the limitation of CMIP5 outputs and thus we used the mean GPP estimated by eq. (S2.4) [i.e., $s\mathrm{GPP}_m(i,j,t,f)$] to approximate the vegetation status. Specifically, we had

$$d\mathrm{GPP}_m(i,j,t,f) = a_0 + \mathrm{f(PASW)} + \mathrm{f(TAS)} + \mathrm{f(HURS)} + \mathrm{f(RSDS)} + \mathrm{f(PR)} + \mathrm{f(Veg)}, \quad \text{(S4.1)}$$

where

$$\mathrm{f(PASW)} = a_{11}\, d\mathrm{PASW}_m(i,j,t,f) + a_{12}\, s\mathrm{PASW}_m(i,j,t,f) + a_{13}\, d\mathrm{PASW}_m(i,j,t,f)\, s\mathrm{PASW}_m(i,j,t,f) \quad \text{(S4.2)}$$

$$\mathrm{f(TAS)} = a_{21}\, d\mathrm{TAS}_m(i,j,t,f) + a_{22}\, s\mathrm{TAS}_m(i,j,t,f) + a_{23}\, d\mathrm{TAS}_m(i,j,t,f)\, s\mathrm{TAS}_m(i,j,t,f), \quad \text{(S4.3)}$$

$$\mathrm{f(HURS)} = a_{31}\, d\mathrm{HURS}_m(i,j,t,f) + a_{32}\, s\mathrm{HURS}_m(i,j,t,f) + a_{33}\, d\mathrm{HURS}_m(i,j,t,f)\, s\mathrm{HURS}_m(i,j,t,f), \quad \text{(S4.4)}$$

$$\mathrm{f(RSDS)} = a_{41}\, d\mathrm{RSDS}_m(i,j,t,f) + a_{42}\, s\mathrm{RSDS}_m(i,j,t,f) + a_{43}\, d\mathrm{RSDS}_m(i,j,t,f)\, s\mathrm{RSDS}_m(i,j,t,f), \quad \text{(S4.5)}$$

$$\mathrm{f(PR)} = a_{51}\, d\mathrm{PR}_m(i,j,t,f) + a_{52}\, s\mathrm{PR}_m(i,j,t,f) + a_{53}\, d\mathrm{PR}_m(i,j,t,f)\, s\mathrm{PR}_m(i,j,t,f), \quad \text{(S4.6)}$$

$$\mathrm{f(Veg)} = a_{61}\, s\mathrm{GPP}_m(i,j,t,f). \quad \text{(S4.7)}$$

We used the proportion of variance (R^2) explained by the multilinear region in eq. (S4.1) to assess the overall contribution of climate variables and vegetation states for drought month m as defined by PASW of PFT f. For easier presentation, we calculated a single value of R^2 for a specific 25 year period weighted by the number of droughts events across different months and PFTs.

To estimate the overall impact of all climate variables, we calculated the R^2 of the following model,

$$d\mathrm{GPP}_m(i,j,t,f) = a_0 + \mathrm{f(PASW)} + \mathrm{f(TAS)} + \mathrm{f(HURS)} + \mathrm{f(RSDS)} + \mathrm{f(PR)}. \quad \text{(S4.8)}$$

To estimate the impact of individual climate variables, we calculated the R^2 of the following models,

$$d\mathrm{GPP}_m(i,j,t,f) = a_0 + \mathrm{f(PASW)}, \quad \text{(S4.9)}$$

$$d\mathrm{GPP}_m(i,j,t,f) = a_0 + \mathrm{f(TAS)}, \quad \text{(S4.10)}$$

$$d\mathrm{GPP}_m(i,j,t,f) = a_0 + \mathrm{f(HURS)}, \quad \text{(S4.11)}$$

$$d\mathrm{GPP}_m(i,j,t,f) = a_0 + \mathrm{f(RSDS)}, \quad \text{(S4.12)}$$

$$d\mathrm{GPP}_m(i,j,t,f) = a_0 + \mathrm{f(PR)}. \quad \text{(S4.13)}$$

$$d\mathrm{GPP}_m(i,j,t,f) = a_0 + \mathrm{f(Veg)}. \quad \text{(S4.14)}$$

Supplementary Note 5: Statistical tests

5.1 Statistical tests for drought-associated GPP reductions

We assumed that there were two types of errors associated the estimated drought-associated GPP reductions at the global scale. The first type of error comes from the error in estimation from our smooth spline (e_{sp}). The second type of error comes from the model structure (e_{md}). In order to test if the drought associated GPP reduction are significantly different between periods p_1 and p_0 , we decomposed the GPP reduction using the follow equation,

$$d\mathrm{GPP}(p_1,k) = d\mathrm{GPP}(p_0,k) + \Delta d\mathrm{GPP}(p_1,p_0) + e_{\mathrm{md,GPP}}(p_0,p_1,k) + e_{\mathrm{sp,GPP}}(p_1,k) \quad \text{(S5.1)}$$

where $d\mathrm{GPP}(p\ ,k)$ is the estimated GPP reduction by a specific type of droughts (e.g., mild, moderate and extreme droughts) during period p for model *k*. $\Delta d\mathrm{GPP}(p_1,p_0)$ is the difference in drought associated GPP reduction between periods p_0 and p_1. $e_{\mathrm{md,GPP}}(p_0,p_1,k)$ is the random error in $\Delta d\mathrm{GPP}(p_1,p_0)$ due to model structure difference. To relax the impact of parametric distribution on the statistical tests, we assumed that $e_{\mathrm{md,GPP}}(p_0,p_1,k)$ followed an empirical cumulative distribution function (ECDF) estimated from the deviation of ensemble mean for each model. Namely,

$$e_{\mathrm{md,GPP}}(p_0,p_1,k) \sim \ \mathrm{ECDF}(\hat{d}\mathrm{GPP}(p_1,k) - \hat{d}\mathrm{GPP}(p_0,k))\ \{k = 1,...,N_{md}\} \quad \text{(S5.2)}$$

where N_{md} is the total number of models. We assumed a Gaussian distribution for $e_{\mathrm{sp,GPP}}(p,\mathrm{k})$ in view that deviations from the fitted spline of GPP generally followed a Gaussian distribution. Namely, we have

$$e_{\mathrm{sp,GPP}}(p_1,k) \sim \mathrm{G}(0,\ \delta_{sp,\mathrm{GPP}}{}^2(p_1,k)) \quad \text{(S5.3)}$$

with $\delta_{\mathrm{sp,GPP}}{}^2(p_1,k)$ estimated from eq. (S2.5).

Meanwhile, the drought-associated GPP reduction during period p_0 for model *k* in eq. (S5.1), $d\mathrm{GPP}(p_0,k)$, was decomposed as follows,

$$d\mathrm{GPP}(p_0,k) = d\mathrm{GPP}(p_0) + e_{\mathrm{md,GPP}}(p_0,k) + e_{\mathrm{sp,GPP}}(p_0,k), \quad \text{(S5.4)}$$

where $d\mathrm{GPP}(p_0)$ is the "true" GPP reduction for period p_0. $e_{\mathrm{md,GPP}}(p_0,k)$ is the error in GPP reduction results from model structure for period p_0. Similar to $e_{\mathrm{md,GPP}}(p_0,p_1,k)$ in eq. (S5.1), we assumed that $\mathrm{e}_{\mathrm{md,GPP}}(p_0,k)$ followed an empirical cumulative distribution function (ECDF) estimated from the deviation of ensemble mean for each model. Namely,

$$\mathrm{e}_{\mathrm{md,GPP}}(p_0,k) \sim \ \mathrm{ECDF}(\hat{d}\mathrm{GPP}(p_0,\mathrm{k}))\ \{k = 1,...,N_{md}\} \quad \text{(S5.5)}$$

Similar to eq. (S5.3), we assumed a Gaussian distribution for $e_{\mathrm{sp,GPP}}(p_0,\mathrm{k})$. Combining eqs. (S5.1) and (S5.4), we had

$$d\mathrm{GPP}(p_1,k) = d\mathrm{GPP}(p_0) + \Delta d\mathrm{GPP}(p_1,p_0) + \mathrm{e}_{\mathrm{md,GPP}}(p_0,k) + \mathrm{e}_{\mathrm{md,GPP}}(p_0,p_1,k) + e_{\mathrm{sp,GPP}}(p_0,\mathrm{k}) + e_{\mathrm{sp,GPP}}(p_1,\mathrm{k}). \quad \text{(S5.6)}$$

Under the null hypothesis that there is no difference in drought-associated GPP reduction between period p_0 and p_1, we have

$$\Delta d\mathrm{GPP}(p_1,p_0) = 0. \quad \text{(S5.7)}$$

Based on eq. (S5.1) and (S5.4), the ratio of $d(p_1,k)$ to $d(p_0,k)$ under null hypothesis [$\tau^{(0)}$] can be calculated as follows,

$$\tau^{(0)} = \frac{\sum_{k=1}^{N_{md}} \frac{d\mathrm{GPP}(p_0) + e_{\mathrm{md,GPP}}(p_0,k) + \mathrm{e}_{\mathrm{md,GPP}}(p_0,p_1,k) + e_{\mathrm{sp,GPP}}(p_0,k) + e_{\mathrm{sp,GPP}}(p_1,k)}{d\mathrm{GPP}(p_0) + e_{\mathrm{md,GPP}}(p_0,k) + e_{\mathrm{sp,GPP}}(p_0,k)}}{N_{md}}. \quad \text{(S5.8)}$$

In order to test if there is a significant difference in drought-associated GPP reduction between the two periods, we estimated the sample cumulative probability distribution of $\tau^{(0)}$, $\hat{F}(\tau^{(0)})$, by drawing 10,000 samples for $\tau^{(0)}$. Then the *p*-value of our hypothesis test was calculated as follows,

$$p = \hat{F}(\tau^{(0)} \geq \hat{\tau}), \quad \text{(S5.9)}$$

with

$$\hat{\tau} = \frac{\sum_{k=1}^{N_{md}} \frac{\hat{d}\mathrm{GPP}(p_1,k)}{\hat{d}\mathrm{GPP}(p_0,k)}}{N_{md}}. \quad \text{(S5.10)}$$

$\hat{d}\mathrm{GPP}(p,k)$ was estimated from eq. (S3.1). The procedure of random sample drawing for $\tau^{(0)}$ is as follows. First, we drew one random sample for $e_{\mathrm{md,GPP}}(p_0,k)$, $e_{\mathrm{md,GPP}}(p_0,p_1,k)$, $e_{\mathrm{sp,GPP}}(p_1,\mathrm{k})$, and $e_{\mathrm{sp,GPP}}(p_0,\mathrm{k})$ [k=1,…, N_{md}] from their specific distributions. The $d(p_0)$ was estimated from the mean values of drought-associated GPP reduction during period p_0 (i.e., $\overline{d}(p_0,k)$). Second, we calculated the test statics $\tau^{(0)}$ from eq. (S5.8). We repeated the above two steps for 10, 000 times and then estimated the p-value from eq. (S5.9).

Based on eqs. (S5.1) and (S5.4), we can construct different statistical metrics (e.g., ratio of percentage reduction for different periods) and testing their significance by drawing random samples given the null hypothesis similar to eq. (S5.7).

5.2 Statistical tests for drought risks

The occurrence probability of a specific drought can be decomposed as follows,

$$\gamma(p_1,k) = \gamma(p_0,k) + \Delta\gamma(p_1,p_0) + \mathrm{e}_{\gamma\,\mathrm{md}}(p_0,p_1,k), \quad \text{(S5.11)}$$

where $\gamma(p,k)$ is the estimated occurrence frequency of a specific type of droughts (e.g., mild, moderate and extreme droughts) for period p of model k. $\Delta\gamma(p_1,p_0)$ is the drought frequency difference between periods p_0 and p_1. $\mathrm{e}_{\gamma\,\mathrm{md}}(p_0,p_1,k)$ is the error associated with $\Delta\gamma(p_1,p_0)$ due to model structure differences. Meanwhile, the term $\gamma(p_0,k)$ in eq. (S5.11) was decomposed as follows,

$$\gamma(p_0,k) = \gamma(p_0) + \mathrm{e}_{\gamma\,\mathrm{md}}(p_0,k), \quad \text{(S5.12)}$$

where $\gamma(p_0)$ is the "true" frequency with a specific type of droughts (e.g., mild, moderate and extreme) for period p_0. $\mathrm{e}_{\gamma\,\mathrm{md}}(\mathrm{p},k)$ is the error associated with model structures. Combining eqs. (S5.11) and (S5.12), we had

$$\gamma(p_1,k) = \gamma(p_0) + \mathrm{e}_{\gamma\,\mathrm{md}}(p_0,k) + \Delta\gamma(p_1,p_0) + \mathrm{e}_{\gamma\,\mathrm{md}}(p_0,p_1,k)\ . \tag{S5.13}$$

To relax the impact of parametric distribution on the statistical tests, we assumed that $\mathrm{e}_{\gamma\,\mathrm{md}}(p_1,k)$ and $\mathrm{e}_{\gamma\,\mathrm{md}}(p_0,p_1,k)$ followed an empirical cumulative distribution function (ECDF) estimated from the deviation of ensemble mean from for each model. Namely,

$$\mathrm{e}_{\gamma\,\mathrm{md}}(\mathrm{p},k) \sim \ \ \mathrm{ECDF}(\hat{\gamma}(p,\mathrm{k}) - \overline{\gamma}(p))\ \ \{k = 1,...,N_{md}\}, \tag{S5.14}$$

and

$$\mathrm{e}_{\gamma\,\mathrm{md}}(p_0,p_1,k) \sim \ \ \mathrm{ECDF}(\hat{\gamma}(p_0,k) - \hat{\gamma}(p_1,k) - (\overline{\gamma}(p_0) - \overline{\gamma}(p_1)))\ \ \{k = 1,...,N_{md}\}, \tag{S5.15}$$

where $\overline{\gamma}(p)$ is the mean drought occurrence frequency across models at time period p and N_{md} is the total number of models.

In order to test if the drought occurrence frequency in the future during years 2075-2099 (period p_1) is statistically significant from the past during years 1850-1999 (period p_0), we checked the mean ratio of drought reduction for period p_1 to that for period p_0 as follows,

$$\tau = \frac{\sum_{k=1}^{N_{md}} \frac{\hat{\gamma}(p_1,k)}{\hat{\gamma}(p_0,k)}}{N_{md}} = \frac{\sum_{k=1}^{N_{md}} \frac{\gamma(p_0) + \mathrm{e}_{\gamma\,\mathrm{md}}(p_0,k) + \Delta\gamma(p_1,p_0) + \mathrm{e}_{\gamma\,\mathrm{md}}(p_0,p_1,k)}{\gamma(p_0) + \mathrm{e}_{\gamma\,\mathrm{md}}(p_0,k)}}{N_{md}}. \tag{S5.16}$$

Under the null hypothesis that there is no difference in drought occurrence frequency between period p_0 and p_1, we had

$$\Delta\gamma(p_1,p_0) = 0 \tag{S5.17}$$

Thus, the ratio under null hypothesis can be estimated as follows,

$$\tau^{(0)} = \frac{\sum_{k=1}^{N_{md}} \frac{\gamma(p_0) + \mathrm{e}_{\gamma\,\mathrm{md}}(p_0,k) + \mathrm{e}_{\gamma\,\mathrm{md}}(p_0,p_1,k)}{\gamma(p_0) + \mathrm{e}_{\gamma\,\mathrm{md}}(p_0,k)}}{N_{md}}. \tag{S5.18}$$

In order to test if there is a significant difference in drought occurrence between the two periods, we estimated the sample cumulative probability distribution of $\tau^{(0)}$, $\hat{F}(\tau^{(0)})$, by drawing 10000 samples for $\tau^{(0)}$. Then the *p*-value of our hypothesis test was calculated as follows,

$$p = \hat{F}(\tau^{(0)} \geq \hat{\tau}), \tag{S5.19}$$

with

$$\hat{\tau} = \frac{\sum_{k=1}^{N_{md}} \frac{\hat{\gamma}(p_1,k)}{\hat{\gamma}(p_0,k)}}{N_{md}}. \tag{S5.20}$$

$\hat{\gamma}(p,k)$ is the estimated drought occurrence frequency during period p for model k. The specific procedure of random sample drawing for $\tau^{(0)}$ is as follows. First, we drew one random sample for $\mathrm{e}_{\gamma \mathrm{md}}(p_1,k)$ and $\mathrm{e}_{\gamma \mathrm{md}}(p_0,k)$ [k=1,…, N_{md}] from their specific Gaussian distributions. $\gamma(p_0)$ was estimated from the mean values of drought-associated GPP reduction during period p_0 (i.e., $\overline{\gamma}(p)$). Second, we calculated the test statics $\tau^{(0)}$ from eq. (S5.18). We repeated the above two steps for 10, 000 times and estimated the p-values from eq. (S5.19).

The approach laid out in this section can be similarly applied to other variables that do not contain the error resulting from spline estimation as we did not assume any parametric distributions for the structural error term.

Supplementary Note 6: Soil moisture limitation functions in Earth System Models

Function 1: soil moisture factor $\beta = \frac{1}{(1.0 - e^{-b|\bar{\theta}_s - \theta_w|})}$, where θ_w is the wilting soil moisture for plants ; Ψ_o is the soil water potential that plant's stomata fully open; $\bar{\theta}_s$ is the mean soil moisture in the rooting zone; b is a constant coefficient. β is applied to the canopy stomatal conductance (m/s). See Abramopoulos et al.[4] and Friends and Kiang[5] for details.

Function 2: soil moisture factor $\beta = \sum_{l=1}^{N_l} r(l) \min(\frac{\theta_s(l) - \theta_w}{\theta_o - \theta_w}, 1.0)$, where θ_w is the wilting soil water content for plants ; $\theta_s(l)$ is the soil water content at soil layer l; θ_o is the soil water content that plants fully open their stomata; $r(l)$ is the root fraction in the soil layer l; N_l is the number of soil layers. β is applied to the maximum photosynthetic capacity . See Bonan [6], Cox et al [7] and Krinner et al[8] for details.

Function 3: soil moisture factor with $\beta = 2\delta - \delta^2$ with $\delta = \sum_{l=1}^{N_l} r(l) \min(1.0, \frac{\theta_s(l) - \theta_w}{\theta_f - \theta_w})$, where θ_w is the wilting soil water content for plants ; $\theta_s(l)$ is the soil water content at soil layer l; θ_f is the soil water content at field capacity; $r(l)$ is the root fraction in the soil layer l; N_l is the number of soil layers. β is applied to the maximum photosynthetic capacity as represented by maximum carboxylation rate, $V_{c,max}$ (μmol CO_2/m^2 leaf/s). See Arora[9] for details.

Function 4: soil moisture factor $\beta = \sum_{l=1}^{N_l} r(l) \max(\frac{\Psi_w - \Psi_s(l)}{\Psi w - \Psi_o}, 0)(\frac{\theta_{sat}(l) - \theta_{ice}(l)}{\theta_{sat}(l)})$, where Ψ_w is the wilting soil water potential (Mpa) for plants ; Ψ_o is the soil water potential that plants fully open their stomata; $\Psi_s(l)$ is the soil water potential (Mpa) at soil layer l; $\theta_{sat}(l)$ is the saturated

volumetric water content; $\theta_{ice}(l)$ is the water-equivalent volumetric content for ice; $r(l)$ is the root fraction in the soil layer l; N_l is the number of soil layers. β is applied to the maximum photosynthetic capacity as represented by maximum carboxylation rate, $V_{c,max}$ (μmol CO_2/m^2 leaf/s). See Oleson et al. [10] for details.

Function 5: soil moisture factor $\beta = \frac{ET_d}{ET_s}$, where ET_d is the water demand based on air humidity and photosynthesis; and ET_s is the water supply from soil depending on plant wilting moisture, current soil water availability and plant structural parameters (root density, plant height, sapwood mass, root and xylem conductance). β is applied to the canopy stomatal conductance (m/s). See Milly et al [11] for details.

Function 6: soil moisture factor $\beta = \sum_{l=1}^{N_l} r(l) \max(\frac{\Psi_w - \Psi_s(l)}{\Psi_w}, 0)$, where Ψ_w is the wilting soil water potential (Mpa) for plants ; $\Psi_s(l)$ is the soil water potential (Mpa) at soil layer l; $r(l)$ is the root fraction in the soil layer l; N_l is the number of soil layers. β is applied to the canopy stomatal conductance (m/s). See Abramopoulos et al [4] for details.

Function 7: soil moisture factor $\beta = \min(\max(\frac{\theta_s(1) - \theta_w}{\theta_o - \theta_w}, \frac{\theta_s(2) - \theta_w}{\theta_o - \theta_w}), 1.0)$, where θ_w is the wilting soil water content for plants ; $\theta_s(l)$ is the soil water content at soil layer l (l=1 for soil layer at top 50 cm, l = 2 for soil layer at 50-100cm); θ_o is the soil water content that plants fully open their stomata. β is applied to the maximum photosynthetic capacity . See Sato et al [12] for details.

Supplementary Note 7: Root distributions in Earth System Models

7.1: GFDL model

The root distribution in GFDL land model follows an exponential distribution[13]. Specifically, the root cumulative density function, $f(z)$, is as follows,

$$f(z) = \lambda e^{-\lambda} \qquad \text{(S7.1)}$$

where λ is a PFT specific parameter that determine the shape of root distributions. λ is set as 3.85 for grass, crops and pastures; 6.25 for cold evergreen trees and 3.45 for temperature deciduous and 3.85 for tropical evergreen. The CMIP5 outputs of PFT fractions do not differentiate between different types of trees. Therefore, we used the vegetation map from Milly et al[11] to mask out the cold evergreen trees and use an average value of 3.64 (λ) for all other trees as their root distributions are fairly close. We do acknowledge that there are potential distribution changes of the cold evergreen trees in the future simulations; however, we expect that the impact will be small as the future change are small compared to the overall distribution[11].

7.2: GISS model

The cumulative root distribution in GISS land model follows a power function as follows,

$$F(z) = \begin{cases} az^b & az^b < 1.0 \\ 1.0 & az^b \geq 1.0 \end{cases} \qquad \text{(S7.2)}$$

where a and b is set as 12.5 and 0.9 for tundra, 0.9 and 0.9 for grasses, 0.8 and 0.4 for shrubs, 0.25 and 2.0 for woodland, deciduous and evergreen trees, and 1.1 and 0.4 for rainforests, respectively.

7.3: HadGEM2 model

The root distribution in HadGEM2 model also follows an exponential distribution as specified in eq. (S6.1). The parameter λ is set as 0.67 for broad leaf trees, 2.0 for needle leaf trees, and 4 for grasses and shrubs[14].

7.4: INMCM model

The root distribution in INMCM land model follows a step function[15,16]. The root density is set as 5 for the top 10 cm and 1 for other 10-cm layers. The root depth varies across different PFTs. In this study, we set it as 0.5 meter for grass and crops, and 2.0 meter for shrubs, and 1.0 for trees based on the values of majority of PFTs within grass, shrubs or trees as CMIP5 did not output the PFT fractions.

7.5: MIROC model

MIROC model does not explicitly simulate the root distribution[12]. Instead, it uses the maximum of soil water availability among two soil layers: 1-50cm or 50-100cm. Therefore, wet set the root distribution as 1.0 for first layer (0-50cm) and 0 for second layer (50-100cm) if there is more water in first layer. If there is more soil water in the second layer, then we set root distribution as 0.0 for first layer and 1.0 for second layer.

7.6: NorESM model

The root distribution in NorESM follows an exponential distribution as described in the Community Land Model (CLM)[17]. The root fraction in each soil layer ($r(z)$) is calculated using the following equation,

$$r(z) = \begin{cases} 0.5(e^{-aZ_{h,i-1}} + e^{-bZ_{h,i-1}} - e^{-aZ_{h,i}} + e^{-bZ_{h,i}}) & i < N_s \\ 0.5(e^{-aZ_{h,i-1}} + e^{-bZ_{h,i-1}}) & i = N_s \end{cases} \quad \text{(S7.3)}$$

where $z_{h,i}$ is the depth from soil surface to the interface between soil layer *i* and *i*+1. The values of *a* and *b* for 17 PFTs were obtained from Table 8.3 from CLM technique note[17].

Supplementary Table 1 | Earth System Models and their configurations used in this study

Model Name	Full Name	Institute	Fire	Res.	N[*1]	Dynamic vegetation	Soil moisture function[*2]	Land Model	Source
GFDL-ESM2G	Geophysical Fluid Dynamics Laboratory Earth System Model with Generalized Ocean Layer Dynamics (GOLD) component	Geophysical Fluid Dynamics Laboratory	Yes	144x90	No	Yes	5	LM3.0	[11,18,19]
GFDL-ESM2M	Geophysical Fluid Dynamics Laboratory Earth System Model with Modular Ocean Model version 4.1	Geophysical Fluid Dynamics Laboratory	Yes	144x90	No	Yes	5	LM3.0	[11,18,19]
GISS-E2-H	NASA Goddard Institute for Space Studies Model E, version 2, coupled with HYCOM ocean model	NASA Goddard Institute for Space Studies	No	144x90	No	No	6	GISS-LS	[5,20-22]
GISS-E2-H-CC	NASA Goddard Institute for Space Studies Model E, version 2, coupled with HYCOM ocean model, with an interactive carbon cycle	NASA Goddard Institute for Space Studies	No	144x90	No	No	6	GISS-LS	[5,20-22]
GISS-E2-R	NASA Goddard Institute for Space Studies Model E, version 2, coupled with the Russel ocean model	NASA Goddard Institute for Space Studies	No	144x90	No	No	6	GISS-LS	[5,20-22]
GISS-E2-R-CC	NASA Goddard Institute for Space Studies Model E, version 2, coupled with the Russel ocean model, with an interactive carbon cycle	NASA Goddard Institute for Space Studies	No	144x90	No	No	6	GISS-LS	[5,20-22]
HadGEM2-CC	Hadley Global Environment Model, version 2 - Carbon Cycle	Met Office Hadley Centre	No	192x145	No	Yes	2	MOSES II /TRIFFID	[5,20-22]
HadGEM2-ES	Hadley Global Environment Model, version 2 - Earth System	Met Office Hadley Centre	No	192x145	No	Yes	2	MOSES II/ TRIFFID	[5,20-22]
INMCM4	Numerical Mathematics Climate Model, version 4.0	Numerical Mathematics Climate Model, version 4.0	No	180x120	No	Yes	2	-	[15,16,23]
IPSL-CM5A-LR	Institut Pierre-Simon Laplace Coupled Model, version 5, coupled with NEMO, low resolution	Institut Pierre Simon Laplace Climate Modelling Centre	Yes	96x96	No	Yes	2	ORCHIDEE	
IPSL-CM5A-MR	Institut Pierre-Simon Laplace Coupled Model, version 5, coupled with NEMO, medium resolution	Institut Pierre Simon Laplace Climate Modelling Centre	Yes	144x143	No	Yes	2	ORCHIDEE	[8,24]
IPSL-CM5B-LR	Institut Pierre-Simon Laplace Coupled Model, version 5 with new atmospherical physics, low resolution	Institut Pierre Simon Laplace Climate Modelling Centre	Yes	96x96	No	Yes	2	ORCHIDEE	[8,24]
MIROC-ESM	Model for Interdisciplinary Research on Climate, Earth System Model	Japan Agency for Marine-Earth Science and Technology, Atmosphere and Ocean Research Institute, and National Institute for Environmental Studies	No	128x64	No	Yes	7	MATSIRO/ SEIB-DGVM	[12,25]
MIROC-ESM(CHEM)	Model for Interdisciplinary Research on Climate, Earth System Model with an atmospheric chemistry component (CHASER 4.1)	Japan Agency for Marine-Earth Science and Technology, Atmosphere and Ocean Research Institute, and National Institute for Environmental Studies	No	128x64	No	Yes	7	MATSIRO/ SEIB-DGVM	[12,25]
NorESM1-M	Norwegian Earth System Model, intermediate resolution	EarthClim	Yes	144x96	Yes	No	4	CLM4	[26,27]
NorESM1-ME[*3]	Norwegian Earth System Model, intermediate resolution with biogeochemical cycling	EarthClim	Yes	144x96	Yes	No	4	CLM4	[26,27]

Notes: 1-Whether the model incorporates nutrient dynamics; 2- See Supplementary Note 6 for details of the soil moisture limitation functions.

References

1 Welch, B. L. The Generalization of Students Problem When Several Different Population Variances Are Involved. *Biometrika* **34**, 28-35, doi:Doi 10.2307/2332510 (1947).

2 Chambers, J. M. & Hastie, T. *Statistical models in S*. (Wadsworth & Brooks/Cole Advanced Books & Software, 1992).

3 Eubank, R. L. Diagnostics for Smoothing Splines. *Journal of the Royal Statistical Society. Series B (Methodological)* **47**, 332-341, doi:10.2307/2345576 (1985).

4 Abramopoulos, F., Rosenzweig, C. & Choudhury, B. Improved Ground Hydrology Calculations for Global Climate Models (GCMs): Soil Water Movement and Evapotranspiration. *J Climate* **1**, 921-941, doi:Doi 10.1175/1520-0442(1988)001<0921:Ighcfg>2.0.Co;2 (1988).

5 Friend, A. D. & Kiang, N. Y. Land surface model development for the GISS GCM: Effects of improved canopy physiology on simulated climate. *J Climate* **18**, 2883-2902, doi:Doi 10.1175/Jcli3425.1 (2005).

6 B.Bonan, G. A land surface model (LSM version 1.0) for ecological, hydrological, and atmospheric studies: Technical description and user's guide., 150 (National Center for Atmospheric Research, Boulder, CO, 1996).

7 Cox, P. M. *et al.* The impact of new land surface physics on the GCM simulation of climate and climate sensitivity. *Clim Dyn* **15**, 183-203, doi:DOI 10.1007/s003820050276 (1999).

8 Krinner, G. *et al.* A dynamic global vegetation model for studies of the coupled atmosphere-biosphere system. *Glob Biogeochem Cycle* **19**, doi:10.1029/2003gb002199 (2005).

9 Arora, V. K. Simulating energy and carbon fluxes over winter wheat using coupled land surface and terrestrial ecosystem models. *Agric For Meteorol* **118**, 21-47, doi:10.1016/S0168-1923(03)00073-X (2003).

10 Oleson, K. W. *et al.* Technical description of version 4.0 of the Community Land Model (CLM). 257 (National Center for Atmospheric Research, Boulder, CO, 2010).

11 Milly, P. C. D. *et al.* An Enhanced Model of Land Water and Energy for Global Hydrologic and Earth-System Studies. *J Hydrometeorol* **15**, 1739-1761, doi:10.1175/Jhm-D-13-0162.1 (2014).

12 Sato, H., Itoh, A. & Kohyama, T. SEIB-DGVM: A new dynamic global vegetation model using a spatially explicit individual-based approach. *Ecol Model* **200**, 279-307, doi:10.1016/j.ecolmodel.2006.09.006 (2007).

13 Weng, E. S. *et al.* Scaling from individual trees to forests in an Earth system modeling framework using a mathematically tractable model of height-structured competition. *Biogeosciences* **12**, 2655-2694, doi:10.5194/bg-12-2655-2015 (2015).

14 Cox, P. M. Description of the "TRIFFID" Dynamic Global Vegetation Model. Report No. Hadley Centre technical note 24, 16 (Hadley Centre, Met Office, London Road, Bracknell, Berks, RG122SY, UK, 2001).

15 Volodin, E. & Lykosov, V. Parametrization of Heat and Moisture Transfer in the Soil-Vegetation System for Use in Atmospheric General Circulation Models: 2. Numerical Experiments in Climate Modeling. *Izvestia-atmospheric and oceanic physics* **34**, 559-569 (1998).

16 Volodin, E. & Lykosov, V. Parametrization of Heat and Moisture Transfer in the Soil-Vegetation System for Use in Atmospheric General Circulation Models: 1. Formulation and Simulations BAsed on Local Observational Data. *Izvestia-atmospheric and oceanic physics* **34**, 559-569 (1998).

17 Oleson, K. W. *et al.* Technical description of version 4.5 of the Community Land Model (CLM). 420 (National Center for Atmospheric Research, Boulder, CO, 2013).

18 Dunne, J. P. *et al.* GFDL's ESM2 Global Coupled Climate-Carbon Earth System Models. Part II: Carbon System Formulation and Baseline Simulation Characteristics. *J Climate* **26**, 2247-2267, doi:10.1175/Jcli-D-12-00150.1 (2013).
19 Shevliakova, E. *et al.* Carbon cycling under 300 years of land use change: Importance of the secondary vegetation sink. *Global Biogeochem. Cycles* **23**, GB2022, doi:10.1029/2007gb003176 (2009).
20 Schmidt, G. A. *et al.* Configuration and assessment of the GISS ModelE2 contributions to the CMIP5 archive. *J Adv Model Earth Sy* **6**, 141-184, doi:10.1002/2013MS000265 (2014).
21 Schmidt, G. A. *et al.* Present-day atmospheric simulations using GISS ModelE: Comparison to in situ, satellite, and reanalysis data. *J Climate* **19**, 153-192, doi:Doi 10.1175/Jcli3612.1 (2006).
22 Rosenzweig, C. & Abramopoulos, F. Land-surface model development for the GISS GCM. *J Climate* **10**, 2040-2054, doi:Doi 10.1175/1520-0442(1997)010<2040:Lsmdft>2.0.Co;2 (1997).
23 Volodin, E. M., Dianskii, N. A. & Gusev, A. V. Simulating present-day climate with the INMCM4.0 coupled model of the atmospheric and oceanic general circulations. *Izv Atmos Ocean Phy+* **46**, 414-431, doi:10.1134/S000143381004002x (2010).
24 Dufresne, J. L. *et al.* Climate change projections using the IPSL-CM5 Earth System Model: from CMIP3 to CMIP5. *Clim Dyn* **40**, 2123-2165, doi:10.1007/s00382-012-1636-1 (2013).
25 Watanabe, S. *et al.* MIROC-ESM 2010: model description and basic results of CMIP5-20c3m experiments. *Geosci Model Dev* **4**, 845-872, doi:10.5194/gmd-4-845-2011 (2011).
26 Iversen, T. *et al.* The Norwegian Earth System Model, NorESM1-M - Part 2: Climate response and scenario projections. *Geosci Model Dev* **6**, 389-415, doi:10.5194/gmd-6-389-2013 (2013).
27 Bentsen, M. *et al.* The Norwegian Earth System Model, NorESM1-M - Part 1: Description and basic evaluation of the physical climate. *Geosci Model Dev* **6**, 687-720, doi:10.5194/gmd-6-687-2013 (2013).

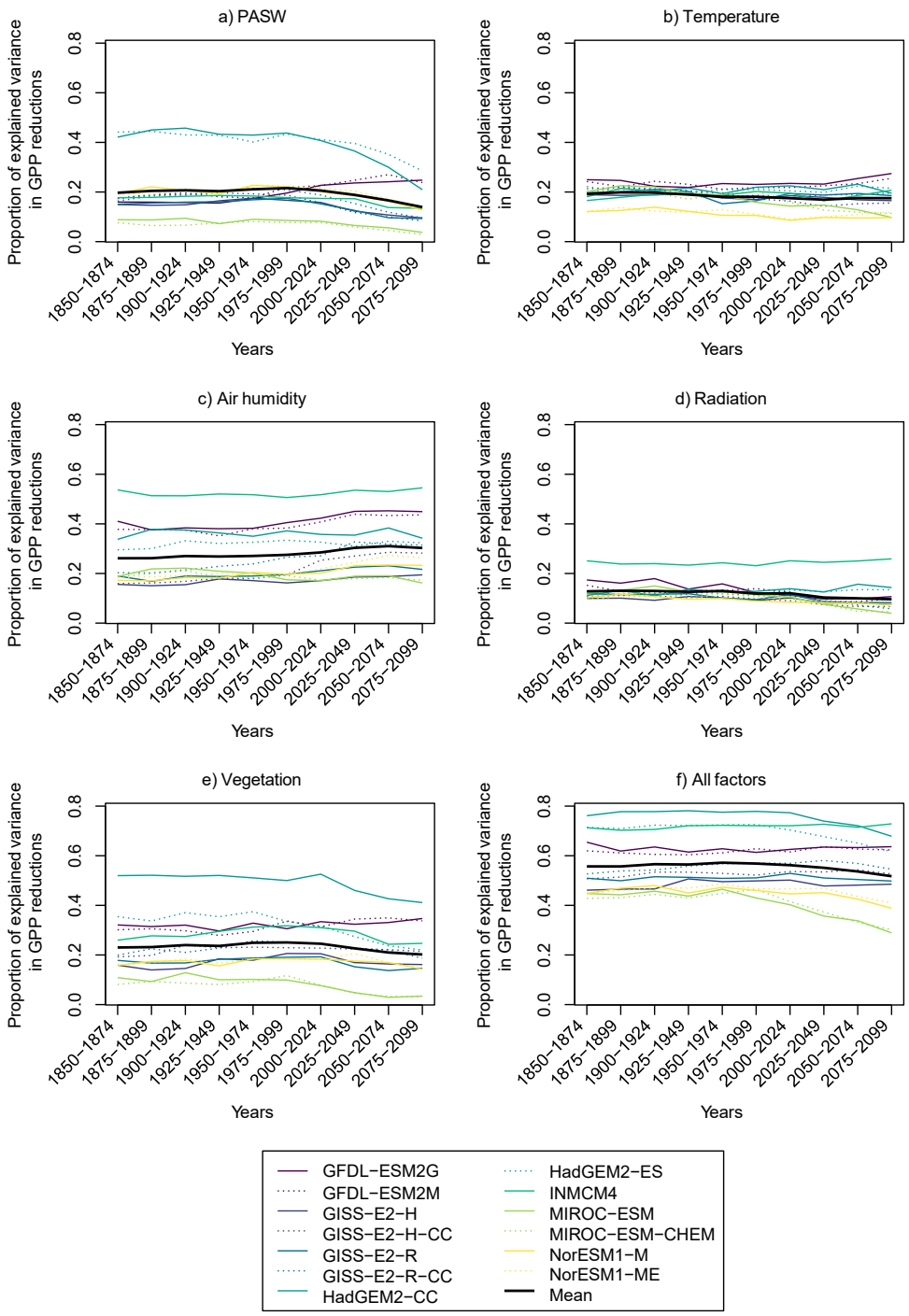

Supplementary Fig. 1 | Temporal Changes in proportion of variance in GPP reductions associated with droughts contributed by different factors under greenhouse gas emission scenario RCP8.5. We considered the contributions by monthly plant accessible soil water (PASW) (a), temperature (b), humidity (c), radiation (d), the vegetation (e), and the combination of all factors (f). See Supplementary Note 4 for details of the calculations.

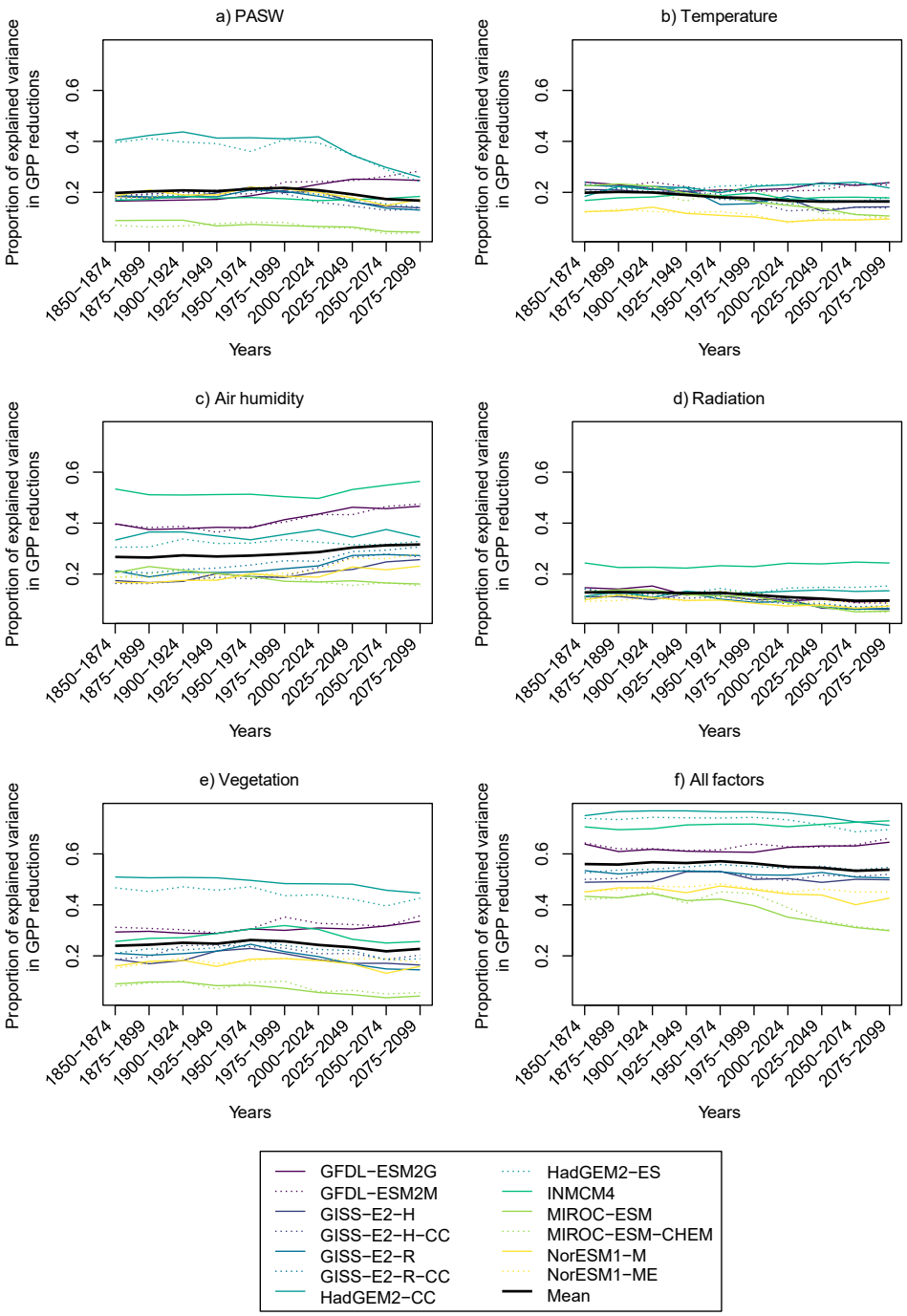

Supplementary Fig. 2 | Temporal Changes in percentage of variance in GPP reductions associated with droughts contributed by different factors under greenhouse gas emission scenario RCP4.5. We considered contributions from monthly plant accessible soil water (PASW) (a), temperature (b), humidity (c), radiation (d), vegetation (e), and the combination of all factors (f). See Supplementary Note 4 for details of the calculations. See Supplementary Table 1 for the abbreviations of 13 selected Earth system models.

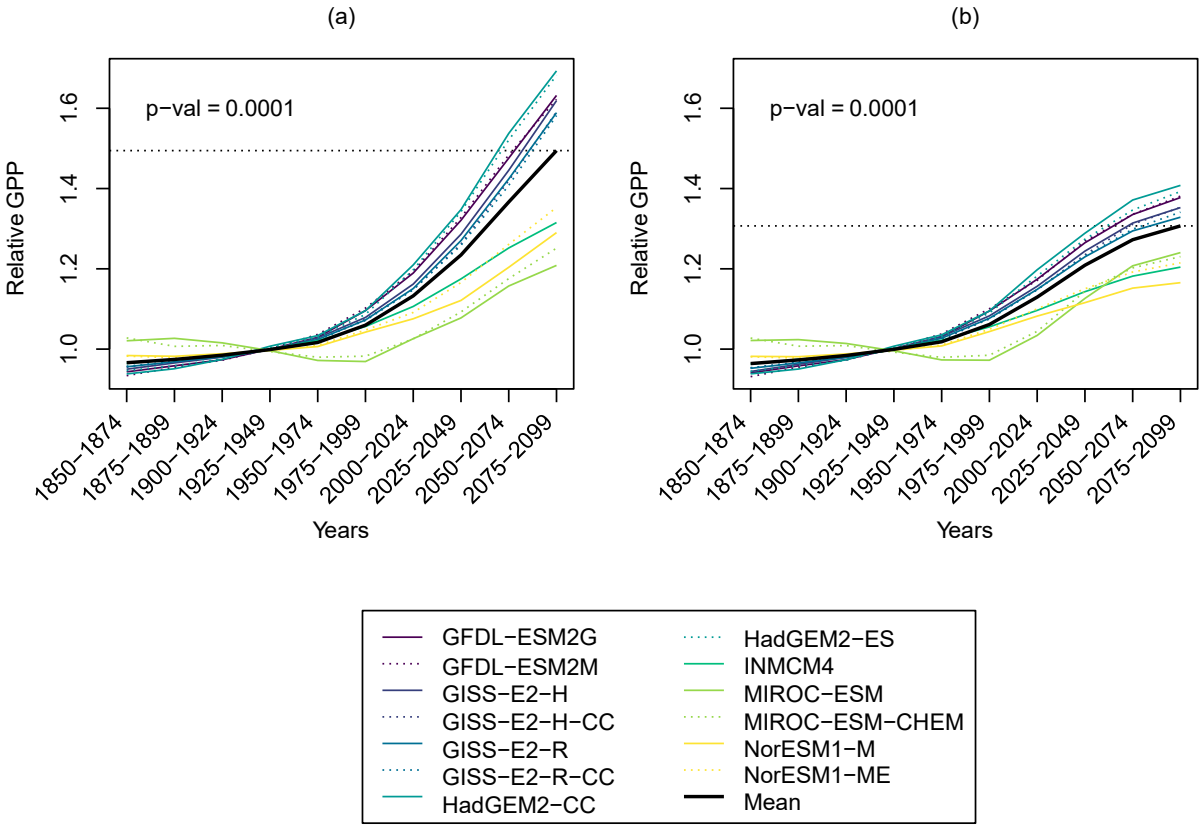

Supplementary Fig. 3 | Temporal changes in mean global GPP relative to the historical period of 1850–1999. We considered both high (RCP 8.5; a) and intermediate (RCP 4.5; b) greenhouse gas emission scenario. The relative GPP was calculated on a model-specific basis, dividing the GPP over a specific period by that over the historical period, projected by 13 Earth System models for the vegetated lands. The p-values were calculated to check if there is a significant difference between future period of 2075–2099 and historical period of 1850–1999 using the approach laid out in Supplementary Note 5.1. See Supplementary Table 1 for the abbreviations of 13 selected Earth system models.

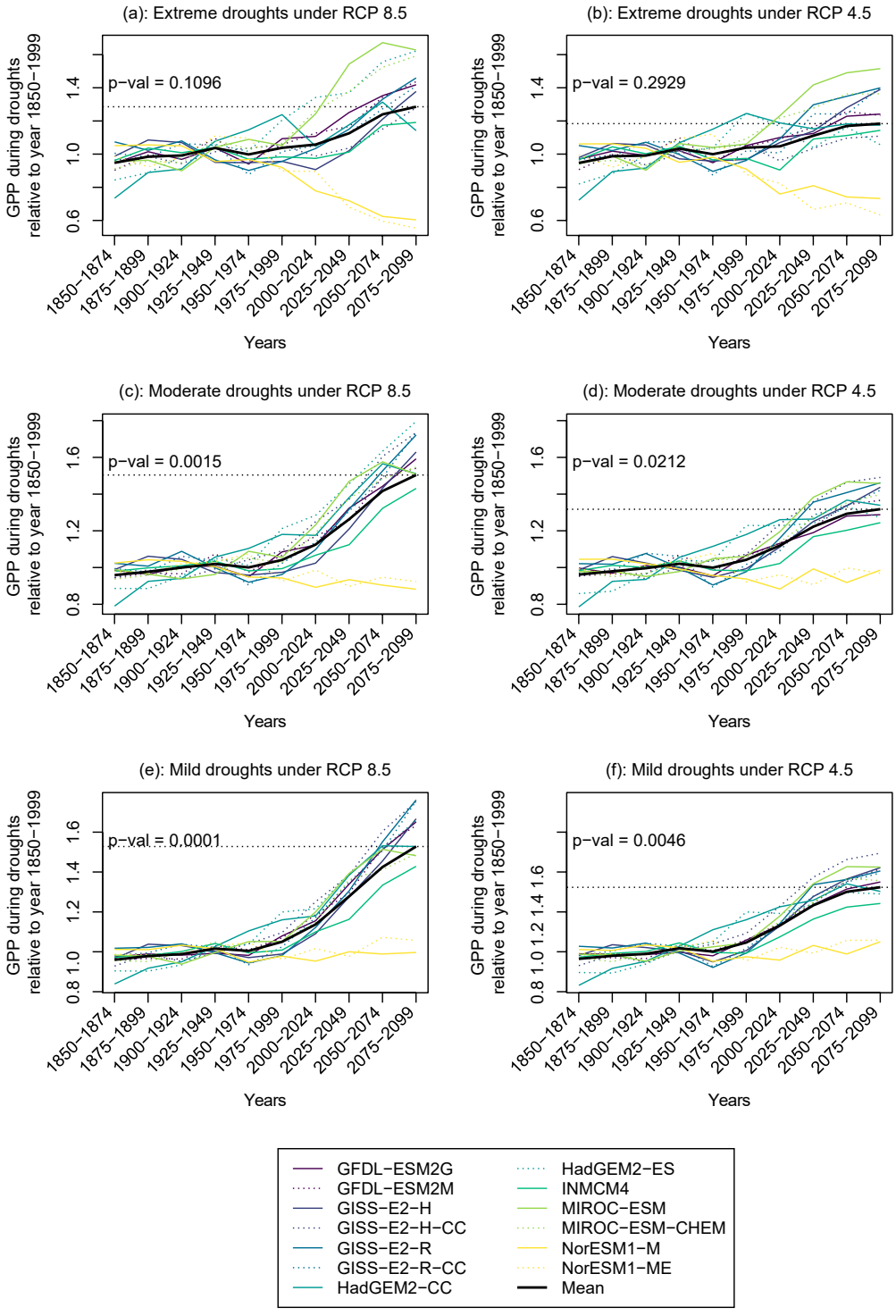

Supplementary Fig. 4 | Temporal changes in mean GPP during drought months (kg C/m^2/month) relative to the historical period of 1850–1999. The relative GPP was calculated on a model-specific basis, dividing the GPP over a specific period by that over the historical period. The p-values were calculated to check if there is a significant difference between future period of 2075–2099 and historical period of 1850–1999 using the bootstrap sampling approach laid out in Supplementary Note 5.2.

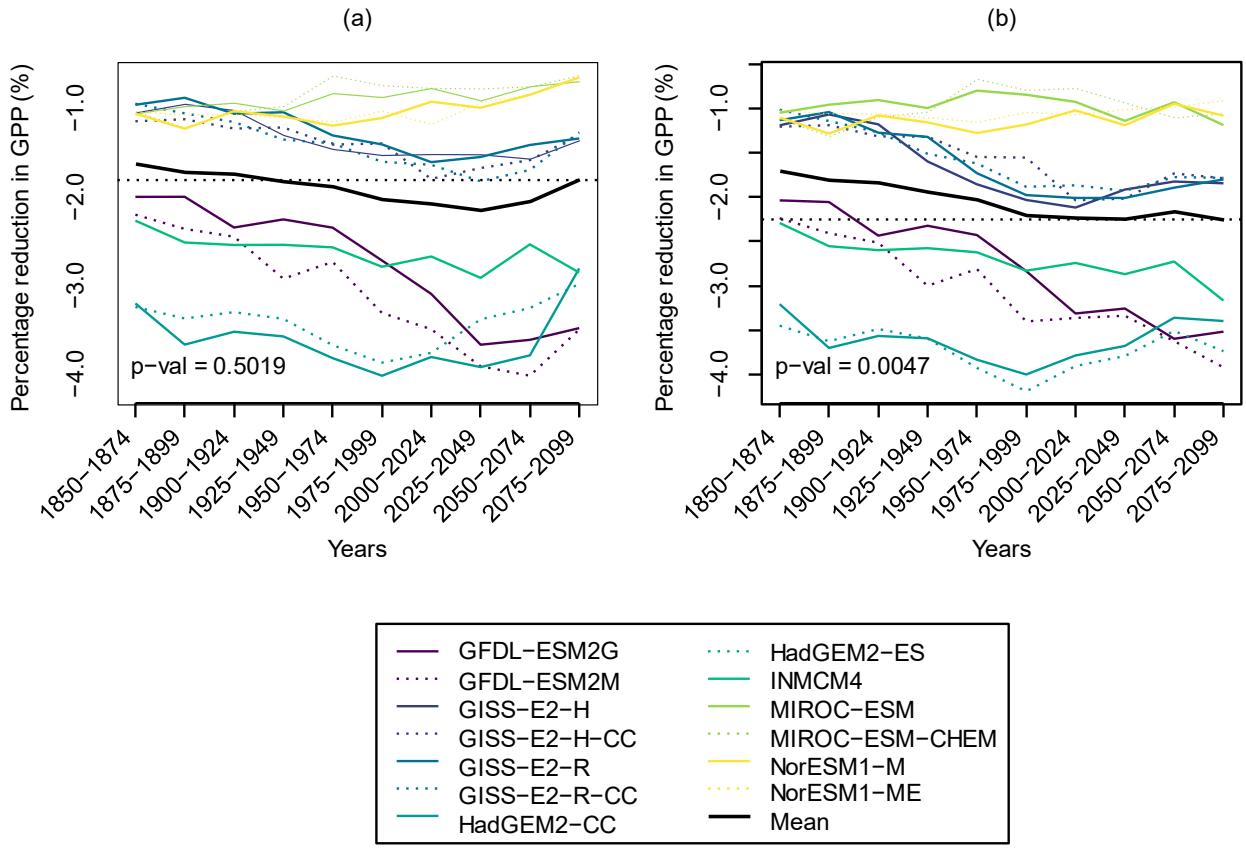

Supplementary Fig. 5 | Temporal changes of percentage reduction in GPP (%) associated with all droughts. We considered GPP reduction under both high (RCP 8.5; a) and intermediate (RCP 4.5; b) greenhouse gas emission scenario, projected by 13 Earth System models over the vegetated lands. The dotted horizontal line shows the mean value during 2075–2099. The p-values were calculated to check if there is a significant difference between future period of 2075–2099 and historical period of 1850–1999 (one side test assuming a larger magnitude of GPP reduction in the future) using the bootstrap sampling approach laid out in Supplementary Note 5.1. See Supplementary Table 1 for the abbreviations of 13 selected Earth system models.

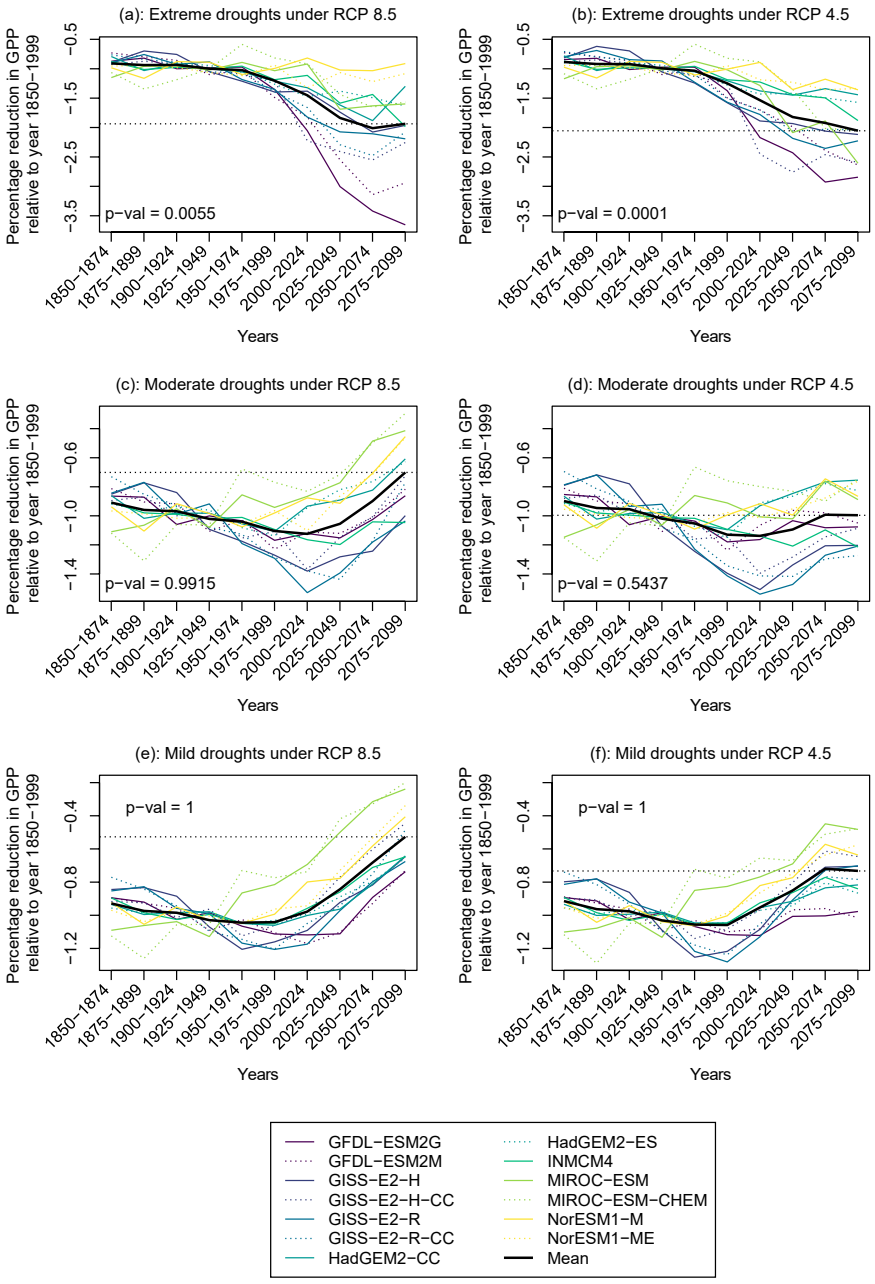

Supplementary Fig. 6 | Temporal changes of percentage reduction in GPP associated with droughts relative to the historical period of 1850–1999. The relative values were calculated on a model-specific basis, dividing percentage change in GPP per year for a specific period by that over the historical period. Positive values indicate droughts increase GPP while negative values indicate droughts decrease GPP. Values of <-1 indicate stronger impact of drought on GPP compared to the historical period; while values >-1 indicate weaker impact of drought. The dotted line shows the mean relative value during 2075–2099. The p-values were calculated to check if the percentage reduction for future period of 2075–2099 is significantly larger than the historical period of 1850–1999 using the bootstrap sampling approach laid out in Supplementary Note 5.1.

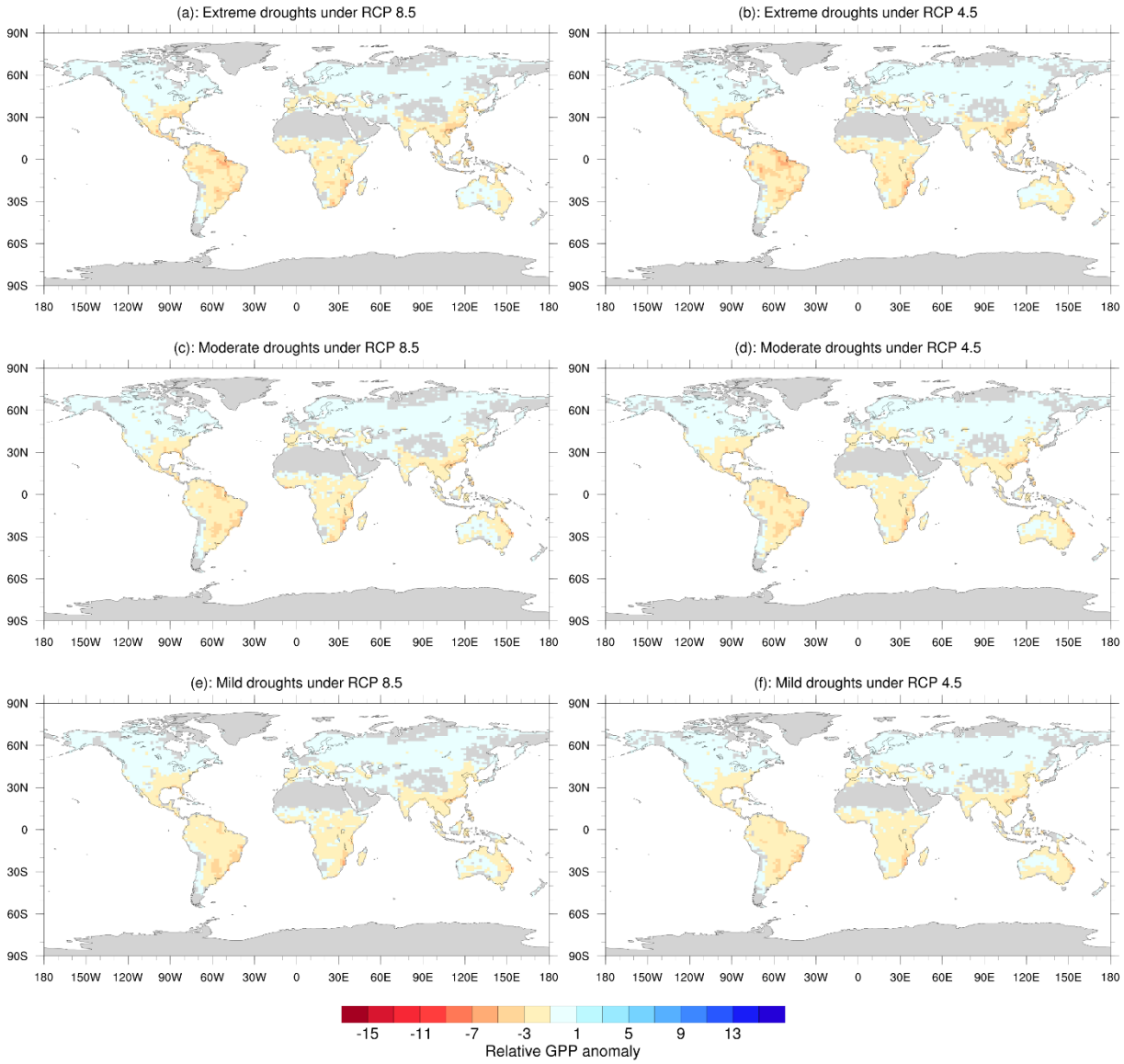

Supplementary Fig. 7 | Spatial distribution of GPP anomalies during 1975-1999 relative to the period of 1850–1999. The relative anomalies were calculated on a model specific basis, dividing grid-cell-specific mean annual GPP anomaly (kg C/m2/ year) during 1975–1999 associated with different types of droughts by the global mean annual GPP reduction over vegetated land (kg C/m2/ year) for the historical period of 1850–1999. The relative anomalies were multiplied by (-1) to indicate that droughts decrease GPP, with -1 indicating the reference global mean GPP reduction for the historical period. Hence, values < -1 (shades of red) indicate that the magnitude of GPP reduction was larger than the global mean GPP reduction during the historical period of 1850–1999, while values > -1 (light blue) indicate that the magnitude of GPP reduction was smaller. The drought-associated changes in GPP projected by different models were interpolated to a reference spatial resolution [1.125 ^{o} (longitude) x 0.9375^{o} (latitude)] for mapping purposes.

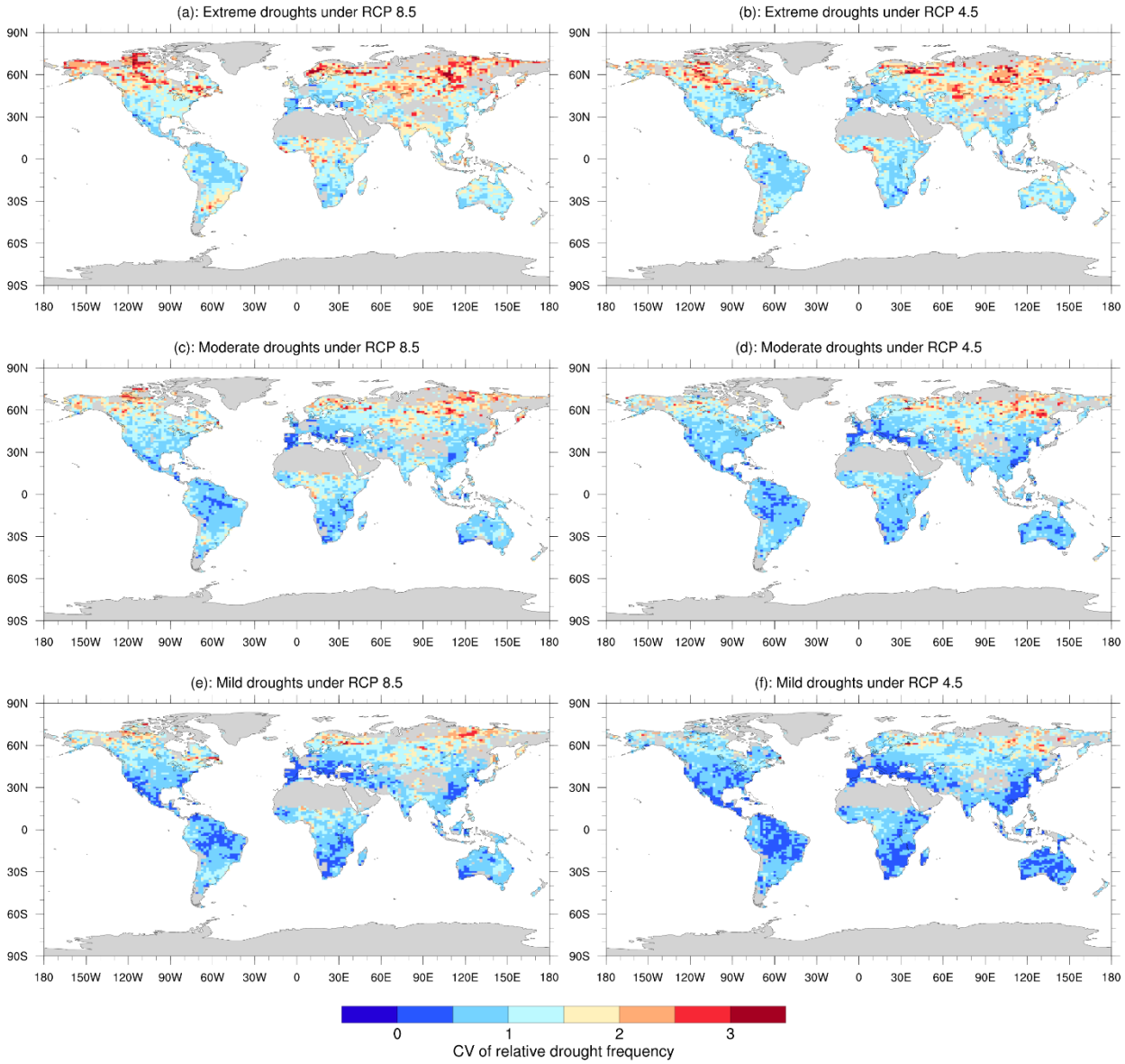

Supplementary Fig. 8 | Maps of coefficient of variation (CV) for drought frequency during 2075–2099 relative to the historical period of 1850–1999. The CV was calculated from the ensemble of 13 ESMs. The relative frequencies were calculated on a model- and grid-cell-specific basis, dividing the mean drought frequency per year (drought events/year) during 2075–2099 by that over the historical period. See Fig. 2 for maps of mean values.

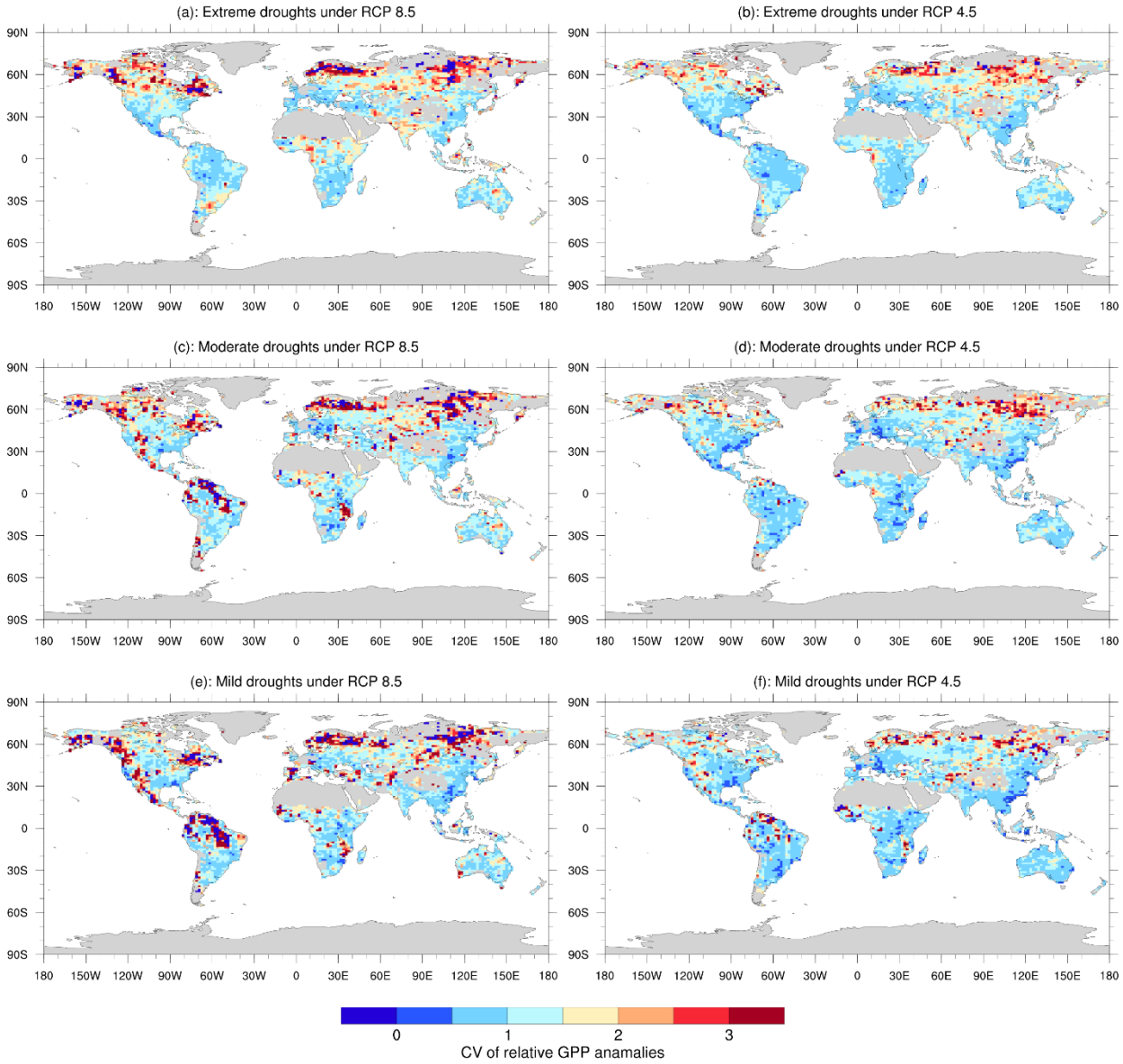

Supplementary Fig. 9 | Maps of coefficient of variation (CV) for anomalies in GPP associated with droughts during 2075–2099 relative to the historical period of 1850–1999. The CV was calculated from the ensemble of 13 Earth System models. The relative anomalies in GPP were calculated on a model specific basis, dividing the grid-cell-specific mean annual GPP change (kg C/m^2/ year) during 2075–2099 by the global mean of annual GPP change (kg C/m^2/ year) over the vegetated land for the historical period of 1850–1999. See Fig. 4 for maps of mean values.

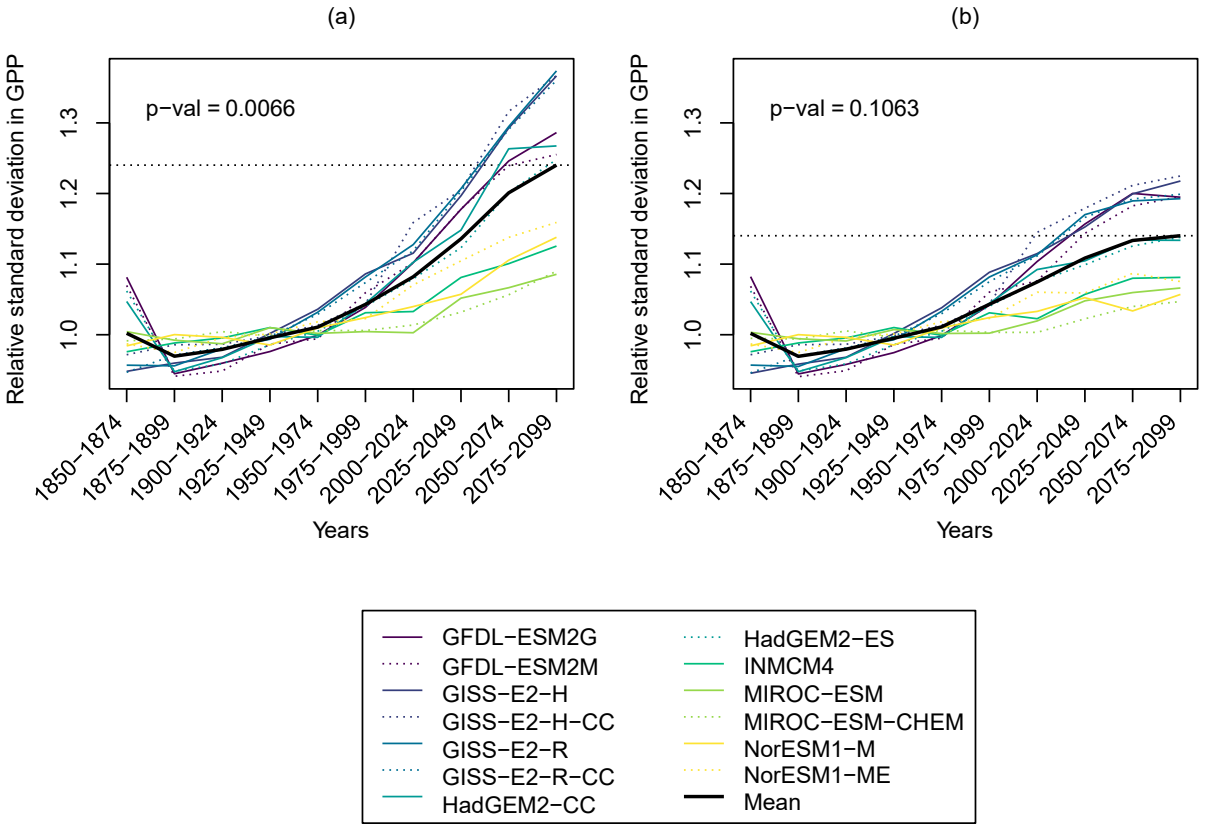

Supplementary Fig. 10 | Temporal change in standard deviation of mean global GPP at different time periods relative to the historical period of 1850–1999. The standard deviations were calculated under both high (RCP 8.5; a) and intermediate (RCP 4.5; b) greenhouse gas emission scenario, aggregated over vegetated lands for each selected Earth System models. The p-values were calculated to check if there is a significant difference between future period of 2075–2099 and historical period of 1850–1999 using the bootstrap sampling approach laid out in Supplementary Note 5.2. See Supplementary Table 1 for the abbreviations of 13 selected Earth system models.

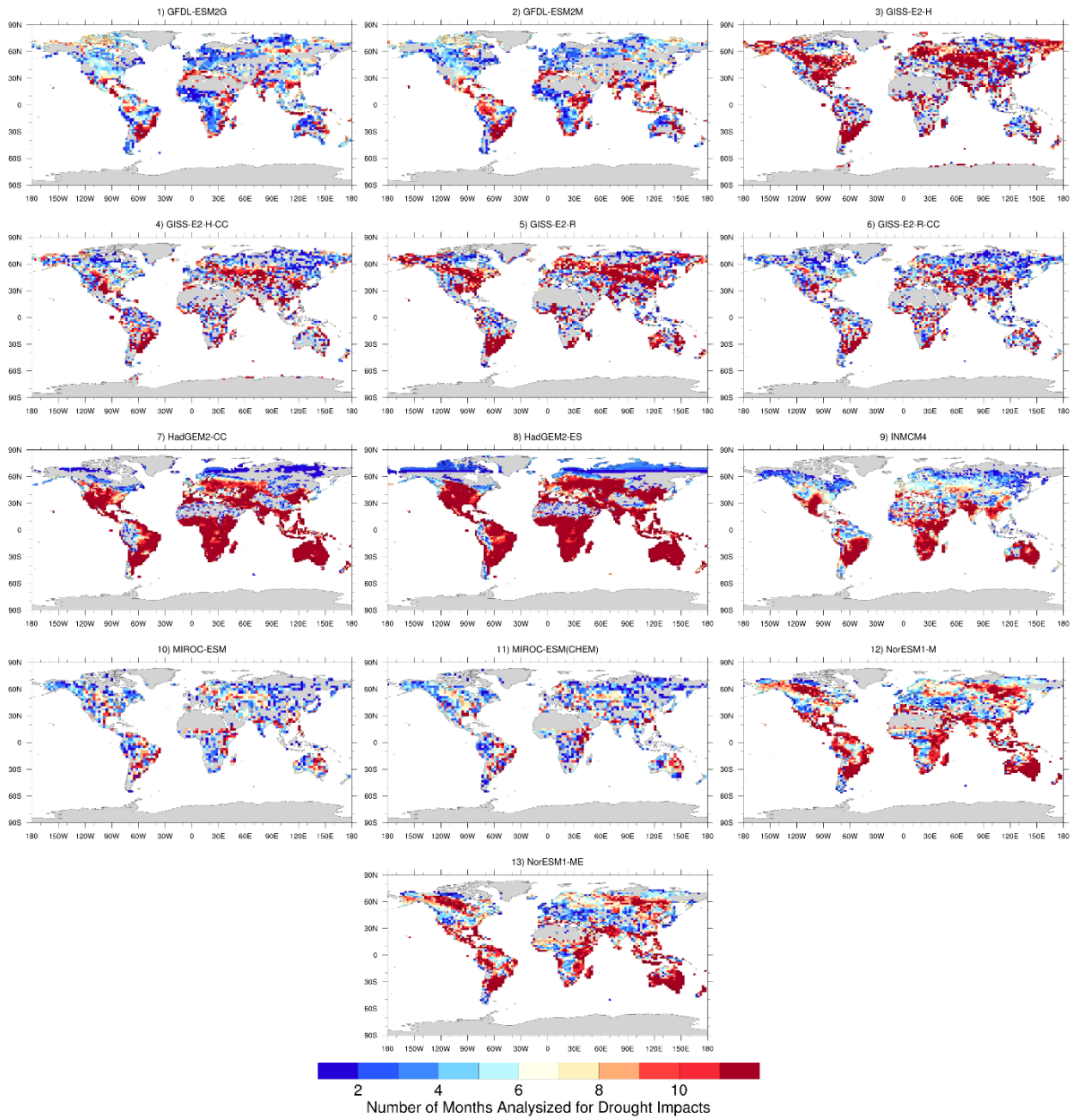

Supplementary Fig. 11 | Spatial distribution in number of months analyzed for drought impacts on GPP projected by 13 Earth System models under greenhouse gas emission scenario RCP 8.5. A month was selected for analysis only if GPP values of this month for the years with PASW less than the10th percentile (defined based on the historical period of 1850–1999) were significantly lower than the rest of years during 1850–2099 at the significance level of 0.01. See Supplementary Note 1 for details of the statistical test.

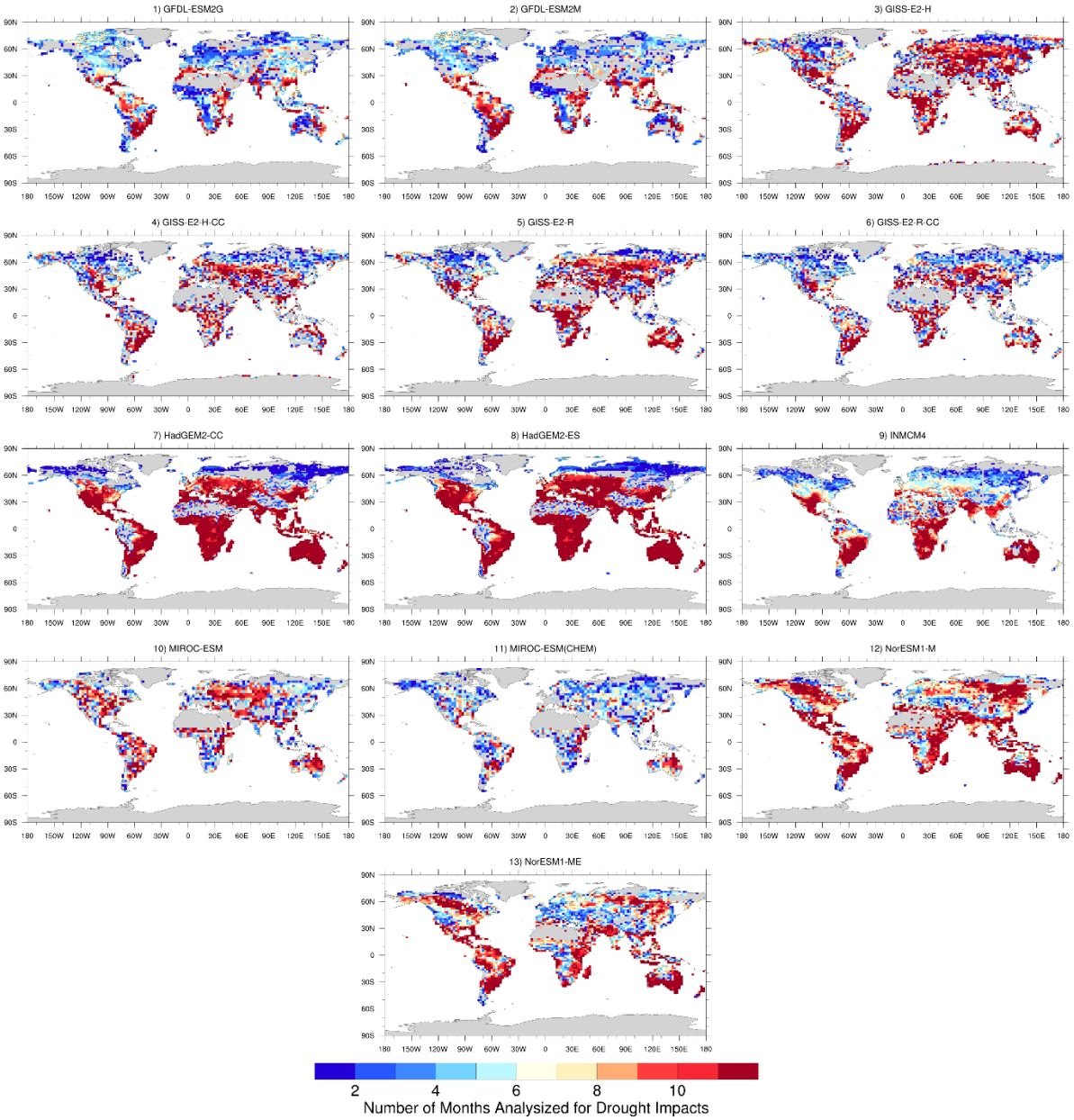

Supplementary Fig. 12 | Spatial distribution in number of months analyzed for drought impacts on GPP projected by 13 Earth System models under greenhouse gas emission scenario RCP 4.5. A month was selected for analysis only if GPP values of this month for the years with PASW less than the10th percentile (defined based on the historical period of 1850-1999) were significantly lower than the rest of years during 1850–2099 at the significance level of 0.01. See Supplementary Note 1 for details of the statistical test.